

The Brazil-nut effect and its application to asteroids

Soko Matsumura,^{1,2*} Derek C. Richardson,² Patrick Michel,³
Stephen R. Schwartz^{3,2} and Ronald-Louis Ballouz²

¹*School of Engineering, Physics, and Mathematics, University of Dundee, Scotland DD1 4HN*

²*Department of Astronomy, University of Maryland, College Park, MD 20741*

³*Lagrange Laboratory, University of Nice-Sophia Antipolis, CNRS, Observatoire de la Côte d’Azur, France*

11 July 2014

ABSTRACT

Out of the handful of asteroids that have been imaged, some have distributions of blocks that are not easily explained. In this paper, we investigate the possibility that seismic shaking leads to the size sorting of particles in asteroids. In particular, we focus on the so-called Brazil Nut Effect (BNE) that separates large particles from small ones under vibrations. We study the BNE over a wide range of parameters by using the N -body code PKDGRAV, and find that the effect is largely insensitive to the coefficients of restitution, but sensitive to friction constants and oscillation speeds. Agreeing with the previous results, we find that convection drives the BNE, where the intruder rises to the top of the particle bed. For the wide-cylinder case, we also observe a “whale” effect, where the intruder follows the convective current and does not stay at the surface. We show that the non-dimensional critical conditions for the BNE agree well with previous studies. We also show that the BNE is scalable for low-gravity environments and that the rise speed of an intruder is proportional to the square root of the gravitational acceleration. Finally, we apply the critical conditions to observed asteroids, and find that the critical oscillation speeds are comparable to the seismic oscillation speeds that are expected from non-destructive impacts.

Key words: methods: numerical – comets: general – minor planets, asteroids: general

1 INTRODUCTION

Asteroids are small rocky bodies left over from the planet formation era. Although their internal structure is not well constrained, the images of a handful of asteroids have provided us with the clues to the origins of their surface features (e.g., Asphaug et al. 2002; Chapman 2004). Perhaps the most prominent feature is craters that indicate the history of impacts by other objects. However, there are other surface features that are more subtle and need explanations.

For example, Asphaug et al. (2001) pointed out that the blocks on (433) Eros do not obey any obvious dynamical distribution such as association with potential source craters or sweep-up correlated with the asteroid rotation. These blocks are likely ejecta fragments, but most of them are not seen with pits that would indicate collisions at meters per second into the low-gravity regolith. They proposed that size sorting in asteroid regolith could explain such a distribution of blocks.

Another potential example of this size sorting is (25143) Itokawa, where smooth and rugged regions are observed.

Miyamoto et al. (2007) proposed that the substantial vibrations and the resulting granular convection could explain such a difference in distributions of particles. Besides the abundance of boulders, Itokawa is also characterized by a lack of major craters (Fujiwara et al. 2006). Since the total volume of boulders on Itokawa is larger than the available volume in the identified craters, all the boulders cannot be from these craters. This may further support the size-sorting scenario on Itokawa. Alternatively, the absence of large fresh craters might be explained if the most recent impact erased its own crater (e.g., Michel et al. 2009). Furthermore, the boulders on Itokawa could also be explained by assuming that Itokawa was made by the reaccumulation of fragments from a catastrophically disrupted parent body (Michel & Richardson 2013). In this paper, we explore whether the size sorting due to global oscillations is possible on asteroids such as Eros and Itokawa.

Asphaug et al. (2001) identified two phenomena in granular systems that might have direct relevance to asteroids. One of them is the inelastic segregation that could form regions of granular solid via the aggregation of inelastically colliding objects. The other is the size segregation via the so-called Brazil Nut Effect (BNE) that describes the rise of

* E-mail: s.matsumura@dundee.ac.uk

a particle embedded in an oscillating system of smaller particles in a confined environment (e.g., Rosato et al. 1987). We focus on this latter effect in this paper. The BNE has been studied in many different setups, but rarely in the low-gravity environments that are relevant to asteroids. There are some recent exceptions, such as Tancredi et al. (2012) and Güttler et al. (2013), and we compare our results with theirs in Sections 3.4 and 3.5.

There are two distinct models of the BNE — one of them is the intruder model, where the number of large particles is small compared to the number of smaller ones, and the other is the binary mixture model, where both small and large particles occupy comparable volumes. These models behave differently under vibrations, partly because interactions between large particles become significant for the latter (e.g., Sanders et al. 2004). The internal structure of asteroids is not well known, and has so far been only guessed at through theoretical and numerical works (e.g., Asphaug et al. 2002; Richardson et al. 2002). Due to this lack of knowledge, we assume in this paper that the intruder model is appropriate for asteroids.

The behavior of the intruder model differs depending on the oscillation speeds (e.g., Kudrolli 2004). When the oscillation is weak, the particles are in the dense limit, where the contacts between particles last for a long time. As the oscillation speed increases, the system can become vibro-fluidized, where the particles behave like a fluid and their interactions can be treated as binary collisions. In the vibro-fluidized limit, the intruder's behavior depends on the size ratio and the density ratio of the constituent particles. The intruder rises to the surface when its density is lower than that of the surrounding smaller particles, and sinks when its density is larger (e.g., Ohtsuki et al. 1995; Hsiau & Yu 1997; Shishodia & Wassgren 2001; Breu et al. 2003; Huerta & Ruiz-Suárez 2004). In the dense limit, the intruder rises independent of the density ratio (e.g., Liffman et al. 2001; Huerta & Ruiz-Suárez 2004). All of our simulations are likely to be in the dense limit most of the time, because most particles have a number of neighboring particles in contact. As we describe in the next section, we use a version of the N -body code PKDGRAV that can handle systems with long-lasting contacts.

In this paper, we investigate the Brazil Nut Effect as a potential mechanism to sort particles in asteroids and to explain distributions of boulders on asteroids' surfaces. The efficiency of the BNE depends on many different parameters; furthermore, those corresponding parameters in asteroids are unknown. Therefore, we first investigate the efficiency of the BNE through a wide range of initial conditions and then apply the model to the low-gravity environments that are suitable for asteroids. In Section 2, we introduce our numerical methods and the choice of initial conditions. In Section 3, we study the dependence of the BNE on various parameters including the coefficients of restitution, the friction constants, the oscillation speeds, and the depth of particle beds (Sections 3.1–3.3). We also compare our models with previous studies and find good agreements (Sections 3.3 and 3.4). The BNE in low-gravity environments is investigated in Section 3.5, and we apply the critical conditions to observed asteroids. Finally in Section 4, we discuss and summarize our study.

2 METHOD

In this section, we introduce our numerical code PKDGRAV (Section 2.1) as well as the initial conditions used for our simulations (Section 2.2).

2.1 Numerical Method: PKDGRAV

PKDGRAV is a parallel N -body gravity tree code (Stadel 2001) adapted for particle collisions (Richardson et al. 2000, 2009, 2011). Originally, collisions in PKDGRAV were treated as idealized single-point-of-contact impacts between rigid spheres. However, such an instantaneous collision assumption is not appropriate for a dense system like a particle bed, where particle contacts can last many timesteps. Recently, Schwartz et al. (2012) added a soft-sphere option to PKDGRAV that handles long-lasting contacts with reaction forces dependent on the degree of overlap (a proxy for surface deformation) and contact history. We use this version of the code for our study of the BNE. The code uses a 2nd-order leapfrog integrator, with accelerations due to gravity and contact forces recomputed each step. Various types of user-definable confining walls are available that can be combined to provide complex boundary conditions for the simulations. For example, we use an infinitely tall cylinder and box as our container, as described in the following subsection. The code also includes an optional variable gravity field based on a user-specified set of rules. This allows us to change the magnitude and a direction of gravity in the simulation (see Section 3.5 for details).

The spring/dash-pot model used in PKDGRAV's soft-sphere implementation is described fully in Schwartz et al. (2012). Briefly, a (spherical) particle overlapping with a neighbor or confining wall feels a reaction force in the normal and tangential directions determined by spring constants (k_n , k_t), with optional damping and effects that impose static, rolling, and/or twisting friction. The damping parameters (C_n , C_t) are related to the conventional normal and tangential coefficients of restitution used in hard-sphere implementations, ϵ_n and ϵ_t . The static, rolling, and twisting friction components are parameterized by dimensionless coefficients μ_s , μ_r , and μ_t , respectively. Plausible values for these various parameters are obtained through comparison with laboratory experiments. Careful consideration of the soft-sphere parameters is needed to ensure internal consistency, particularly with the choice of k_n , k_t , and timestep — a separate code is provided to assist the user with configuring these parameters correctly. For most of our simulations, $k_n = 2.261947 \times 10^9 \text{ g s}^{-2}$ and timestep $1.851201 \times 10^{-6} \text{ s}$ are adopted, which permits a maximum particle speed of 200 cm s^{-1} with no more than 1 % overlap between spheres. As a conservative estimate, we consider a maximum particle speed that is larger than the maximum oscillation speed of our default case of 93.9 cm s^{-1} . For other parameters, μ_t is set to zero all the time for simplicity, while ϵ_n , ϵ_t , μ_s and μ_r are varied over wide ranges. We will investigate the effect of μ_t in future work.

The numerical approach has been validated through comparison with laboratory experiments; e.g., Schwartz et al. (2012) demonstrated that PKDGRAV correctly reproduces experiments of granular flow through cylindrical hoppers, specifically the flow rate as a function

of aperture size, and Schwartz et al. (2013) demonstrated successful simulation of laboratory impact experiments into sintered glass beads using a cohesion model coupled with the soft-sphere code in PKDGRAV. Most recently, Schwartz et al. (2014) applied the code to low-speed impacts into regolith in order to test asteroid sampling mechanism design.

2.2 Initial Conditions

Unless noted otherwise, we use the same particle distributions in an infinitely tall cylinder with a diameter of 10 cm as the initial condition for all our simulations. In our intruder model, there are 1800 small particles and 1 larger particle, where the diameters of small and large particles are $d_s = 1$ cm and $d_l = 3$ cm, respectively. Both types of particles are assumed to have the same mass density of 2.7 g cm^{-3} , which corresponds to the density of aluminium. For our default simulation, we adopt the coefficients of restitution $\epsilon_n = \epsilon_t = 0.5$, static friction $\mu_s = 0.7$, and rolling friction $\mu_r = 0.1$.¹ The choices of parameters are rather arbitrary. However, as we see below, the BNE is relatively insensitive to the exact choice of the coefficients of restitution. The BNE is sensitive to the choice of the friction constants, so we choose the values that result in the occurrence of BNE as default values. In terms of real materials, these constants nearly correspond to the oxidized Al that was used in the experiments of Clément et al. (1992), where they studied a vibrationally excited pile of beads and observed spontaneous heaping and convection. Besides particle-particle interactions that are described above, PKDGRAV also handles particle-wall interactions. We use the same coefficients of restitution and friction constants as the particles for all of the cylinder walls.

The simulations are divided into two stages — the filling of the cylinder with particles, and the oscillation of the filled cylinder. In the first stage, the large particle is initially placed at the floor of the cylinder (whose center is the origin of the coordinate), while small particles are suspended in the air, 10–130 cm above the bottom panel. The free-fall simulation is done under Earth gravity $g = 980 \text{ cm s}^{-2}$, and the cylinder is filled with small particles in ~ 0.5 s. For the low gravity simulations in Section 3.5, this stage is done under the corresponding gravitational environment. Under the influence of Earth gravity, particles fill to a height of just under 22 cm. The schematic figure of our system at the end of the first stage is shown in Figure 1. In the second stage, the entire cylinder is vertically shaken in a sinusoidal manner with a given amplitude A and frequency ω as $z = A \sin(\omega t)$, where z is the height of the base of the cylinder relative to an arbitrary zero point. The default amplitude and frequency are $A = d_s = 1$ cm, and $\omega = 3\sqrt{a_g/A} = 93.9 \text{ rad s}^{-1}$. Here, a_g is a gravitational acceleration, and $a_g = g$ is assumed for most cases except for Section 3.5. Thus, the maximum speed for the default shake is $v_{max} = \omega A = 93.9 \text{ cm s}^{-1}$. Most of

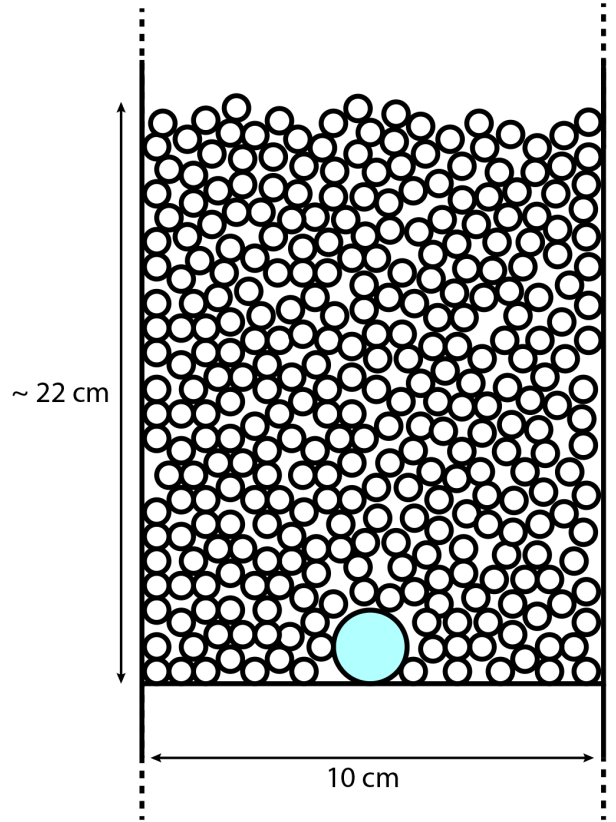


Figure 1. Schematic diagram of a cross-section of the experiment after an infinitely long cylindrical container (with a diameter of 10 cm) is filled up with small particles (up to ~ 22 cm from the origin), but before shaking begins. The large cyan particle (the intruder) is initially located at the floor.

our simulations are done on a single core of a modern CPU such as Intel Xeon and AMD Opteron. For the simulations in this paper, the runtime varied from ~ 10 hours to ~ 10 days for 150 cycles, depending on the number of particles as well as the choice of parameters such as oscillation frequencies. In general, low oscillation frequency simulations take longer than high frequency ones, because a longer time is required to complete 150 cycles of oscillation.

3 RESULTS

In this section, we present the results of our simulations. First, we vary several parameters and investigate how they affect the BNE.

3.1 Dependence on Coefficients of Restitution

In this subsection, we study the dependence of BNE on normal and tangential coefficients of restitution (ϵ_n and ϵ_t , respectively). For all the simulations in this subsection, we assume that the static and rolling friction constants are $\mu_s = 0.7$ and $\mu_r = 0.1$, respectively, and that the oscillation amplitude and frequency are $A = d_s = 1$ cm and $\omega = 3\sqrt{g/d_s} = 93.9 \text{ rad s}^{-1}$, respectively.

¹ We note that ϵ_t used here is not the true tangential coefficient of restitution which is difficult to specify in soft-sphere simulations (see Schwartz et al. 2012). Still, ϵ_t has a one-to-one mapping to a dimensionless quantity C_t as mentioned in Section 2.1 and is defined as $C_t \equiv -2 \ln \epsilon_t \sqrt{k_t \mu / (\pi^2 + (\ln \epsilon_t)^2)}$.

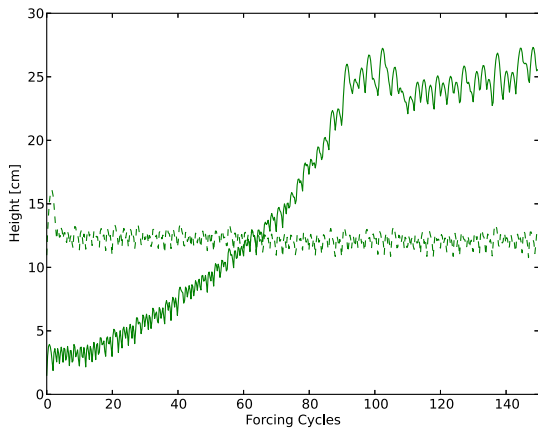


Figure 2. Height evolution of the intruder (solid line) compared with evolution of the median height of the small particles (dashed line). Here, $\epsilon_n = \epsilon_t = 0.5$, $\mu_s = 0.7$ and $\mu_r = 0.1$ are assumed. The intruder rises from the bottom of the cylinder to the surface of the particle bed in ~ 90 cycles.

The height evolution during the oscillation simulation for our default case is shown in Figure 2. The intruder’s height is compared to the median height of small particles \bar{z}_s . After ~ 90 cycles of the oscillations, the intruder rises to the top of the particle bed. Since the height of the particle beds is constantly changing due to oscillations, we define that the intruder arrives at the surface when $z_l > 2\bar{z}_s$. To estimate the variation in our oscillation simulations, we generate 10 independent particle distributions with 1800 small particles and 1 intruder, and perform oscillation simulations by using the same parameters for all of them. For the default parameter set, we find that the average rise cycle (number of oscillations needed for the intruder to rise to the top) is $\bar{\tau}_{cyc} = 92.0$ and the standard deviation is $\sigma = 6.7$.

Now we explore the different sets of restitution coefficients. We change normal and tangential coefficients of restitution from 0.1 – 0.9 with $\Delta\epsilon = 0.1$, and find that the BNE occurs in all of the 81 cases. Moreover, we find that the rise time of an intruder seems relatively independent of the choices of coefficients of restitution. In Figure 3, we compare simulations with $\epsilon_n = 0.5$ and $\epsilon_t = 0.1 - 0.9$ as an example.

To understand this similarity further, we estimate the variations in oscillation simulations by using 10 different particle distributions for 9 different combinations of restitution coefficients $\epsilon_n = \epsilon_t = 0.1 - 0.9$. The mean rise cycle and the standard deviation for each set is compared in the left panel of Figure 4. The mean rise cycle decreases from $\epsilon_n = \epsilon_t = 0.1$ to $\epsilon_n = \epsilon_t = 0.6$ and then slightly increases from $\epsilon_n = \epsilon_t = 0.6$ to $\epsilon_n = \epsilon_t = 0.8$. The rise cycle for $\epsilon_n = \epsilon_t = 0.9$ increases very sharply from $\epsilon_n = \epsilon_t = 0.8$. In fact, the variations of the rise cycles are consistent within 2σ for all the cases except for $\epsilon_n = \epsilon_t = 0.9$.

The right panel of Figure 4 shows the rise cycle estimated for each combination of ϵ_n and ϵ_t by using the same particle distribution. We also plot the mean cycle and the variations estimated from 80 simulations with $\epsilon_n = \epsilon_t = 0.1 - 0.8$. The rise cycles of many combinations appear within 1σ from the mean cycle, and most appear within 2σ . A clear exception is the $\epsilon_n = 0.9$ cases that tend to have shorter rise

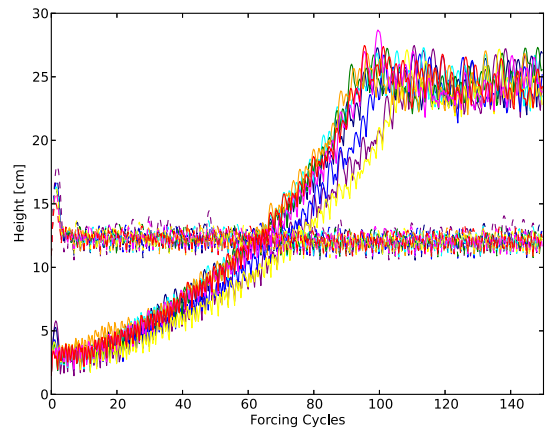


Figure 3. Height evolution of the intruder (solid line) for $\epsilon_n = 0.5$ and $\epsilon_t = 0.1 - 0.9$. All of the rise cycles are consistent with the mean rise cycle determined from the default case within $\sim 3\sigma$, where σ is the default case’s standard deviation that is defined in text. The line colors of red, magenta, orange, yellow, green, cyan, blue, navy, and purple correspond to $\epsilon_t = 0.1 - 0.9$ in an increasing order.

cycles than the others for small values of ϵ_t . There is an indication that the rise time might become shorter for $\epsilon_n = 0.9$ and longer for $\epsilon_t = 0.9$. It is unclear whether this represents poor sampling or a true trend. However, we should note that the BNE does not occur when the collisions are perfectly elastic either in normal or in tangential direction (i.e., either ϵ_n or ϵ_t is 1.0). It is possible that systems with bouncier particles behave differently from those with less elastic ones, because such systems could transit from the dense system to the vibro-fluidized system at a lower oscillation frequency. Since our goal here is to understand the overall trend of the BNE, we defer a more detailed investigation on high values of coefficients of restitution for future work.

The coefficients of restitution for asteroid constituents are not well constrained. Recently, Durda et al. (2011) performed head-on collision experiments between two granite spheres with diameters of 1 m, and estimated that the coefficient of restitution is $\epsilon_n = 0.83 \pm 0.06$ for collision speeds up to $\sim 1.5 \text{ m s}^{-1}$. This normal coefficient of restitution value is relatively large, but is still expected to lead to a general BNE behavior, independent of the value of ϵ_t .

In summary, our results indicate that the BNE is largely independent of the exact choices of coefficients of restitution, except in the most elastic cases. Thus, for the rest of the paper, we assume $\epsilon_n = \epsilon_t = 0.5$ unless it is noted otherwise.

3.2 Dependence on Friction

In this subsection, we study the dependence of BNE on static and rolling friction constants (μ_s and μ_r , respectively). For all the simulations in this subsection, we assume that the normal and tangential coefficients of restitution are $\epsilon_n = \epsilon_t = 0.5$, and that the oscillation amplitude and frequency are $A = d_s = 1 \text{ cm}$ and $\omega = 3\sqrt{g/d_s} = 93.9 \text{ rad s}^{-1}$, respectively.

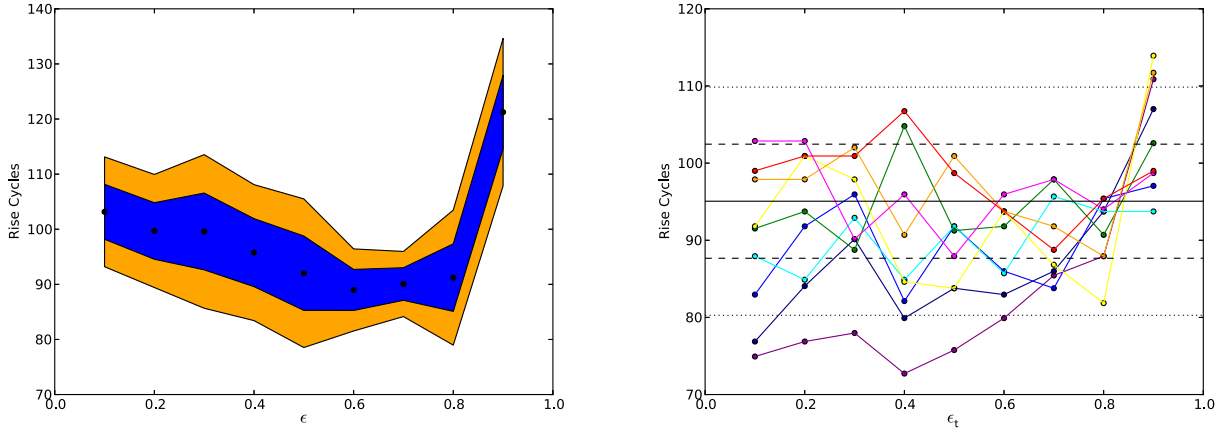


Figure 4. Left: The mean rise cycle (circles) and the standard deviation σ estimated from 10 simulations each for $\epsilon_n = \epsilon_t = 0.1 - 0.9$. The blue and orange regions correspond to 1σ and 2σ , respectively. Except for $\epsilon_n = \epsilon_t = 0.9$, all of these sets have variations in the rise cycles that are consistent within 2σ . Right: the rise cycles for simulations with various ϵ_n and ϵ_t . The red, magenta, orange, yellow, green, cyan, blue, navy, and purple lines correspond to $\epsilon_n = 0.1 - 0.9$ in an increasing order. The black solid, dashed, and dotted lines indicate the mean rise cycle, 1σ , and 2σ estimated from 80 simulations with $\epsilon_n = \epsilon_t = 0.1 - 0.8$.

We change the static friction over $\mu_s = 0.0 - 1.0$ and rolling friction over $\mu_r = 0.0 - 0.2$. We note that, for cohesionless materials, the static friction coefficient is related to the angle of repose of the loose material by $\tan \phi = \mu_s$. Thus, $\mu_s = 1.0$ corresponds to material with a relatively high (45-degree) angle of repose, and sampling from $\mu_s = 0.0$ to 1.0 covers a good range of plausible material properties. The rolling friction does not have as nice a physical correspondence as μ_s , but the friction comes in as a torque due to the normal force acting at a contact point of two particles (Schwartz et al. 2012).

In Figure 5, we plot the instantaneous heights of intruders after 150 oscillations for each simulation. We find that the efficiency of the BNE depends steeply on the friction constants. The figure indicates that the BNE requires a high enough $\mu_s \gtrsim 0.5$ and a low enough $\mu_r \lesssim 0.2$. The difference between non-BNE and BNE regions is illustrated in Figure 6. By dividing the initial distributions of particles into 11 layers (i.e., each layer is ~ 2 cm thick), we plot the height evolution of particles which are initially in the uppermost and lowermost layers, along with that of the intruder particle. There is little vertical mixing of particles when there is no BNE (left panel), while particles are well-mixed when the BNE is observed (right panel). Convection of particles is observed in all the simulations with the BNE, where particles descend along the wall and ascend in the central region. More precisely, small particles follow gradual rise and fall cycles throughout the entire particle distribution while the intruder rises but does not fall. Our results agree with many previous works that have observed convection along with the BNE (e.g., Knight et al. 1993; Pöschel & Herrmann 1995). Furthermore, the trend seen in Figure 5 agrees with the implications of Clément et al. (1992). They experimentally investigated a two-dimensional pile of equal-sized beads under a vertical sinusoidal oscillation, and found that the convection is not observed for polished aluminum beads with $\mu_s = 0.2$, but is observed for oxidized ones with $\mu_s = 0.8$. In their experiments, both kinds of beads have a normal resti-

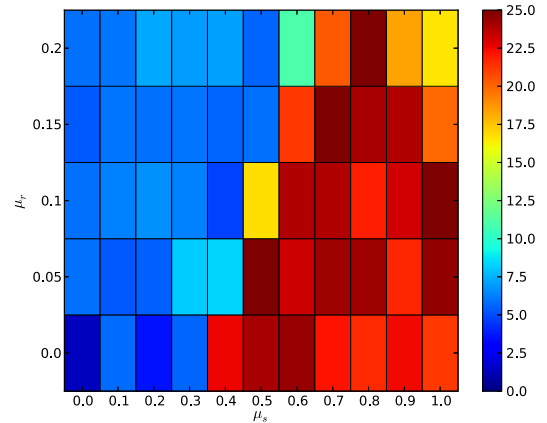


Figure 5. Final intruder heights after 150 oscillations as a function of μ_s and μ_r . Each rectangular region represents a specific choice of μ_s and μ_r and is color coded by the final intruder height (see color legend to the right of the plot). For all the simulations, coefficients of restitution are set to $\epsilon_n = \epsilon_t = 0.5$. There is a sharp transition from no-BNE to BNE regions. A threshold static friction is necessary for the BNE to occur, but high static or rolling friction diminishes the BNE.

tution coefficient of 0.5, which is comparable to our default value. In our simulations, for $\mu_s = 0.2$, the BNE was not observed for any value of μ_r , while for $\mu_s = 0.8$, the BNE was seen for all the values of μ_r we tested.

Convection depends both on particle-particle and on particle-wall frictions. Figure 7 shows cases where particle-particle (left) and particle-wall (right) friction constants are set to zero for our default case. In both cases, convection does not occur and the BNE is severely suppressed compared to the default case in Figure 2, where both of these friction constants have the default values. These figures indicate that

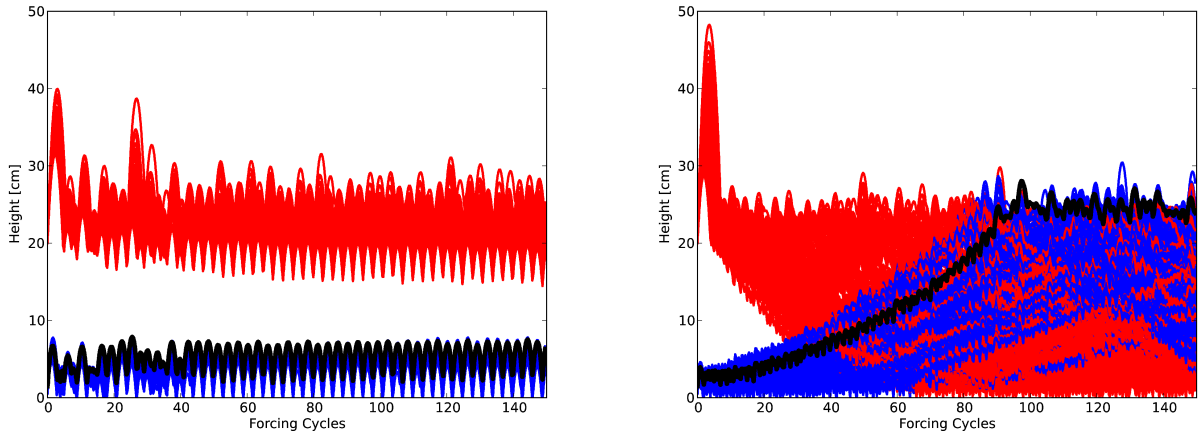


Figure 6. Height evolutions of small particles in the uppermost layer (red) and the lowermost layer (blue) are compared with the corresponding evolution of the intruder (black). All the parameters are the same except that $\mu_s = 0.3$ and $\mu_s = 0.7$ in the left and right panels, respectively. When the BNE does not occur (left), particle layers are well-separated throughout the simulation. On the other hand, when the BNE occurs (right), particle layers are well-mixed due to convection.

kinetic friction (which is related to ϵ_n and ϵ_t) alone is not enough to initiate the BNE.

Figure 5 also indicates that high rolling friction diminishes the BNE. The higher rolling friction means that it is more difficult for particles to rotate with respect to each other. Let us consider three particles lined up side by side. If we move the middle particle upward, then the two neighboring particles start rotating. For higher rolling friction, the energy loss in this process is greater and thus particles tend to lock to each other, which in turn slows down the convection. The slower rise of the intruder in the high-static-friction region is also due to the difficulty of the particles to move relative to one another.

The friction constants of asteroids are even less constrained than the coefficients of restitution. Recently, Yu et al. (2014) performed avalanche experiments of similar-size gravels that were collected from a stream bed, and estimated the restitution coefficients and static constants by using numerical simulations on PKDGRAV. They found $\epsilon_n = \epsilon_t = 0.55$, $\mu_s = 1.31$ and $\mu_r = 3.0$ reproduced their experiments well. These values are not necessarily unique for gravels, but the restitution coefficients are comparable to our default values while the static and rolling frictions are beyond the values we have investigated in this study (see Figure 5). If such gravels represent small particles in asteroids of interest, it would be very difficult to have convection and thus the BNE, because the particles will be simply locked to each other. However, their studies approximate gravels with spheres, and therefore could overestimate these values. More realistic modeling of particles would be necessary in the future. In the rest of the paper, we assume $\mu_s = 0.7$ and $\mu_r = 0.1$ as our default values. Again, $\mu_s = 0.7$ is comparable to the friction constant estimated by Clément et al. (1992) for oxidized Al. Yu et al. (2014) also considered two other types of material: smooth ($\mu_s = \mu_r = 0.0$) and glass ($\mu_s = 0.43$ and $\mu_r = 0.1$). Our default case has the higher static friction than glass but not as high as that of gravel.

3.3 Dependence on Oscillation Speeds and Bed Depths

In this subsection, we study the dependence of the BNE on oscillation amplitude and frequency. For all the simulations in this subsection, we assume $\epsilon_n = \epsilon_t = 0.5$, $\mu_s = 0.7$, and $\mu_r = 0.1$. The oscillation speeds are varied for three different bed depths and two different cylinder widths. The default case of $1800 + 1$ particles in a cylinder with a diameter of 10 cm has a bed depth of ~ 22 cm. The shallower case of $900 + 1$ particles has a depth of ~ 13 cm, and the deeper case of $3600 + 1$ particles has a depth of ~ 47 cm in the same cylinder. We also performed one set of simulations in a wider cylinder with a diameter of 20 cm. That case is comprised of $3600 + 1$ particles and a depth of ~ 13 cm; it can be compared with the shallow-bed case described above.

The final heights of the intruders are plotted for the dimensionless oscillation amplitude $\tilde{A} = 0.5 - 3.0$ and the dimensionless oscillation frequency $\tilde{\omega} = 0.5 - 4.0$ in Figure 8, where

$$\tilde{A} \equiv \frac{A}{d_s}, \quad \tilde{\omega} \equiv \frac{\omega}{\sqrt{g/d_s}}. \quad (1)$$

Since the diameter of a small particle is $d_s = 1$ cm in our simulations, our default case corresponds to $\tilde{A} = 1$ and $\tilde{\omega} = 3$. The left panel of Figure 8 shows our default case with $1800 + 1$ particles and the right panel shows the shallower bed case with $900 + 1$ particles. The result for the deepest bed with $3600 + 1$ particles (not shown here) looks similar to the default case. All of these simulations indicate that the BNE occurs for cases with sufficiently large amplitudes and frequencies. The figure also compares our results with the previous works listed in Table 1. Since every work uses different setups, it is difficult to make a direct comparison. One of the difficulties lies in a density dependence of the BNE. In the vibro-fluidized regime, a high-enough density ratio ρ_l/ρ_s could lead to the reverse BNE, where an intruder sinks to the bottom (e.g., Ohtsuki et al. 1995; Shishodia & Wassgren 2001), while in the dense limit, when particles experience enduring contacts, an intruder appears

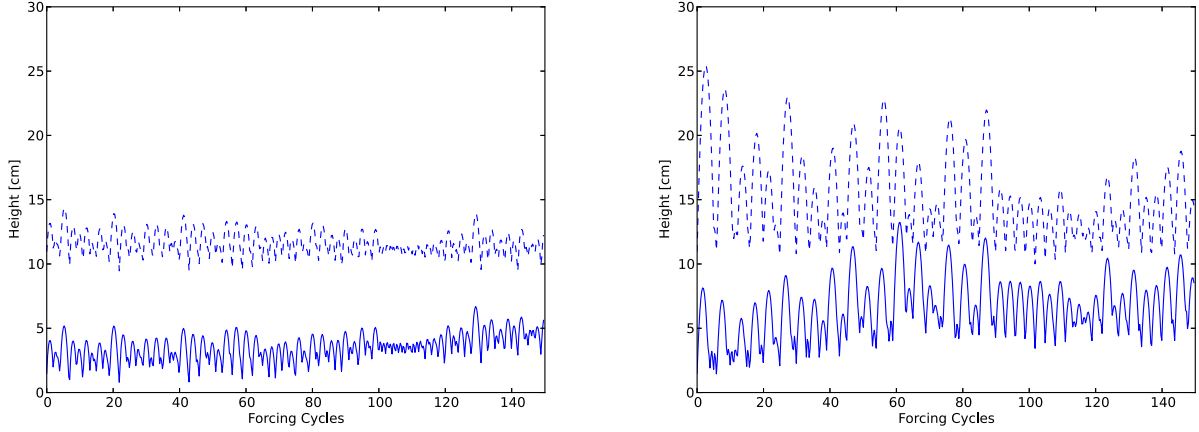


Figure 7. Comparison of the height evolution of the intruder with the median height of the small particles. Left and right panels show the cases where particle-particle frictions are set to zero (left) and particle-wall frictions are set to zero (right), respectively. The other parameters are set to the usual default values.

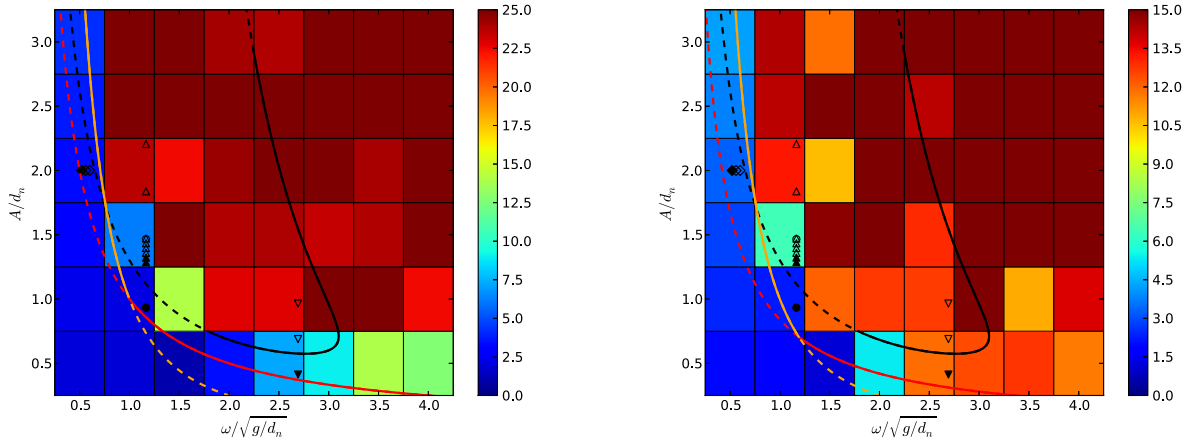


Figure 8. Final intruder heights after 150 oscillations as a function of $\tilde{\omega}$ and \tilde{A} . Each rectangular region represents a specific choice of $\tilde{\omega}$ and \tilde{A} and is color coded by the final intruder height (see color legend to the right of the plot). For all the simulations, $\epsilon_n = \epsilon_t = 0.5$, $\mu_s = 0.7$, and $\mu_r = 0.1$ are assumed. Left and right panels are the cases with $N_s = 1800$ and 900 , respectively. Interior to the black curve is the BNE region estimated from the 2D simulations by Godoy et al. (2008). The dashed part corresponds to the region beyond their investigation. Open and filled symbols are taken from Figure 6 of Godoy et al. (2008) and represent BNE and no-BNE cases, respectively. The circles correspond to the pseudo-2D experiments by Duran et al. (1994), while the downward triangles correspond to the 3D experiments by Knight et al. (1993). The upward triangles and the diamonds are both 2D simulations by Saez et al. (2005) and Pöschel & Herrmann (1995), respectively. Orange and red curves are $\tilde{\Gamma} = 1$ and $\tilde{v} = \tilde{v}_c$, respectively, and the convection is expected above the solid portions of these curves.

to rise independent of the density ratio (e.g., Liffman et al. 2001; Huerta & Ruiz-Suárez 2004). Since we are interested in the standard BNE, we compare our models with previous works that assume comparable densities for small and large particles so that an intruder rises for both the vibro-fluidized regime and the dense limit.

Godoy et al. (2008) selected several investigations that assume the same density for large and small particles, and showed that they all follow similar transition lines that separate BNE and no-BNE regions. These works are also plotted using different symbols in Figure 8. The distribution of open (BNE) and filled (no BNE) symbols agrees well with the general trend of our simulations.

Duran et al. (1994) experimentally studied the BNE in a quasi-two-dimensional bed of aluminum beads, and identified two segregation mechanisms depending on accelerations: arching ($1.0 \lesssim \tilde{\Gamma} \lesssim 1.5$) and convection ($\tilde{\Gamma} \gtrsim 1.5$), where $\tilde{\Gamma} = \tilde{A}\tilde{\omega}^2$ is the dimensionless acceleration. The orange line in Figure 8 corresponds to $\tilde{\Gamma} = 1$; the BNE is expected to take place to the right of this line. The agreement is particularly good for a shallower bed case. The default bed case, however, indicates that $\tilde{\Gamma} \gtrsim 1$ is not a sufficient condition for the BNE.

Hejmady et al. (2012) also experimentally studied the BNE by using a large acrylic disk embedded in a quasi-two-dimensional bed of mustard seeds. They showed that $\tilde{\Gamma} > 1$

Table 1. Model Parameters and Setups

Reference	N_s	ρ_l/ρ_s	d_l/d_s	Restitution coefficients	Friction constants	Type	Shake
Default case of present work	1800	1	3	$\epsilon_n = \epsilon_t = 0.5$	$\mu_s = 0.7, \mu_r = 0.1$	3DS	sinusoidal
Hejmady et al. (2012)		0.30 – 2.34	8.5 – 11.3			2DE	sinusoidal
Godoy et al. (2008)	1200	1	8	$\epsilon_n = \epsilon_t = 0.98$	$\mu_s = \mu_d = 0.7$	2DS	parabolic
Duran et al. (1994)		1	12.9	0.5	0.8	2DE	sinusoidal
Knight et al. (1993)		1	3 – 12.5			3DE	sinusoidal taps
Saez et al. (2005)	3300		13	0.6	0.97	2DS	sinusoidal
Pöschel & Herrmann (1995)	950	1	3.5 – 4.7		0.5	2DS	sinusoidal
Tancredi et al. (2012)	1000	1	3	$\epsilon_n = 0.8 - 0.9, \epsilon_t = 0.95^*$	$\mu_d = 0.6$	3DS	displacements

Column 2: number of small particles, Column 3: density ratio of large to small particles, Column 4: diameter ratio of large to small particles, Column 7: dimension of simulations (S) or experiments (E), Column 8: oscillation type. The value with * is estimated from Figure 4 in Tancredi et al. (2012).

is not a sufficient condition for bulk convection to occur, and proposed that the oscillation speed also needs to exceed some critical value $v_{osc} > v_c$. We estimate the critical oscillation speed for our simulations in Figure 9, where the rise speed of an intruder is plotted as a function of the scaled maximum oscillation speed $\tilde{v}_{osc} = \tilde{A}\tilde{\omega}$ for three different bed depths and two different cylinder widths. Here, the rise speed is defined as the bed depth (defined as $2\tilde{z}_s$) divided by the rise time (determined from the rise cycle defined in Section 3.1). Different from Hejmady et al. (2012), we plot the rise speed instead of the rise time so that \tilde{v}_c is clearly determined from the oscillation speed that corresponds to the zero rise speed. We find that all of these cases have comparable critical speeds. For our default bed depth, we find $\tilde{v}_c \sim 0.97$, while for shallower and deeper bed cases, we find $\tilde{v}_c \sim 0.84$ and 0.91 , respectively. For the case of a shallow-bed in a wide cylinder, we find $\tilde{v}_c \sim 1.04$. These are comparable to the critical value found in Hejmady et al. (2012) ($\tilde{v}_c \sim 1.26$ for $v_c = 16.5 \text{ cm s}^{-1}$). The estimated critical speeds are plotted using red lines in Figure 8. From these figures, we conclude that both $\tilde{\Gamma} \gtrsim 1$ and $\tilde{v}_{osc} \gtrsim \tilde{v}_c$ need to be satisfied for the BNE to take place.

An important indication from Figure 9 is that the rise speed is proportional to the oscillation speed. We will come back to this point in Section 3.5. Furthermore, Figure 9 indicates that there is an optimal bed depth for the BNE, since the rise speed increases from $N_s = 900$ to 1800 , and then decreases from $N_s = 1800$ to 3600 . Such a depth-dependence of the rise time agrees with the recent experimental result by Güttler et al. (2013).

Comparison of the shallow bed case in the default cylinder to that in the wide cylinder (i.e., orange and red lines, respectively) indicates that the BNE may take place slower in a wider cylinder. For the wide-cylinder cases, we find that the convection direction is the same as the default cylinder cases — the particles descend along the wall and ascend near the central region. For the high-end of oscillation speeds, however, we find that the intruder also shows a “whale” effect, where the intruder does not necessarily stay at the top of the cylinder but keeps moving up and down with the convective current. This indicates that the region of the convection roll along the wall is thick enough to pass the intruder downward in the wide-cylinder cases.

We would like to pay a particular attention to the comparison of our work with Godoy et al. (2008). They numeri-

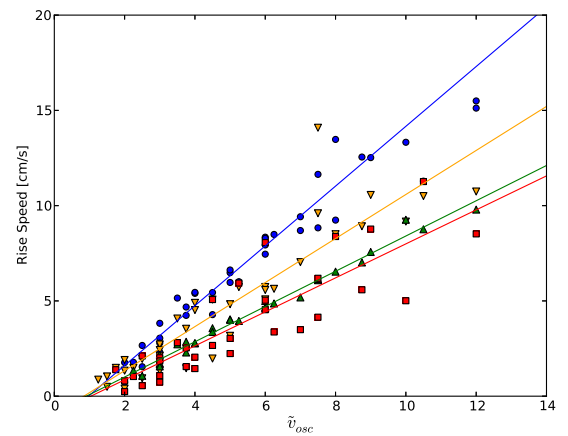


Figure 9. Rise speed compared with the maximum oscillation speed. Blue circles, orange down-pointing triangles, and green up-pointing triangles correspond to the default case ($N = 1800 + 1$), a shallow-bed case ($N = 900 + 1$), and a deep-bed case ($N = 3600 + 1$), respectively. Red squares represent a shallow-bed in a wider cylinder with $N = 3600 + 1$. All of these cases have a similar critical oscillation speed of $\tilde{v}_c \sim 1$. From the best-fit lines, the critical oscillation speeds are $\tilde{v}_c \sim 0.97, 0.84, 0.91$, and 1.04 for each case, respectively. See discussion in Section 3.3.

cally studied the BNE by using the molecular dynamics code developed by Risso et al. (2005). In their simulations, the size ratio of the intruder and surrounding disks is $d_l/d_s = 8$, restitution coefficients $\epsilon_n = \epsilon_t = 0.98$, and static and dynamic friction coefficients $\mu_s = \mu_d = 0.7$. Here, μ_d follows the Coulomb’s law of friction where the magnitude of kinetic friction is independent of speed of slippage. There are 1200 small particles with one intruder, and the 2D box has a width of $40 d_s$. Their oscillations are not sinusoidal, but are given in a periodic vertical parabolic movement with the base acceleration of $\pm \frac{8}{\pi^2} A \omega^2$. Since their acceleration is proportional to the maximum acceleration of the sinusoidal oscillation $A \omega^2$, we expect that our results can be compared to theirs reasonably well.

Instead of changing oscillation amplitude and frequency like we have done in our work, Godoy et al. (2008) varied the dimensionless acceleration and speed which they defined as $\Gamma' = \frac{8}{\pi^2} \tilde{A} \tilde{\omega}^2$ and $\zeta' = \sqrt{2} \tilde{A} \tilde{\omega}$, respectively, and found the

transition line above which the BNE is observed. We also plot their transition line as the black line in Figure 8. The agreement between their simulations and ours is good in the low-frequency region ($\tilde{\omega} \lesssim 2.5$), but our results disagree in the higher frequency region.

There are several possibilities that lead to the difference between our results and those of Godoy et al. (2008). First, our simulations are three-dimensional (3D), while theirs are two-dimensional (2D). However, this is unlikely to be the critical difference, especially since our 3D results agree well with quasi-2D experimental results by Hejmady et al. (2012). Second, we adopt $\epsilon_n = \epsilon_t = 0.5$, while they use $\epsilon_n = \epsilon_t = 0.98$. Kudrolli (2004) proposed a condition that separates the vibro-fluidized regime from the dense regime: $n_{\text{layer}}(1 - \epsilon) < 1$, where n_{layer} is the number of particle layers. According to this condition, our simulations have $n_{\text{layer}} \sim 22$ and $\epsilon = 0.5$ and thus are likely to be in the dense regime of lasting contacts between particles, while their simulations have $n_{\text{layer}} \sim 30$ and $\epsilon = 0.98$ and may be in the vibro-fluidized regime, especially for high accelerations. To address this, we repeated our simulations for $\epsilon_n = \epsilon_t = 0.98$. However, the results are still consistent with $\tilde{\Gamma} \gtrsim 1$ and $\tilde{v}_{\text{osc}} \gtrsim \tilde{v}_c$, rather than with the relation proposed by Godoy et al. (2008). Third, it is possible that our oscillation speeds are too low to turn the BNE off. Thus, we extended our default simulations up to $\tilde{\omega} = 8$ and $\tilde{A} = 4$. However, the BNE is observed for all oscillation speeds we tested. The disagreement may also be due to the differences between our codes, or other differences between our initial setups. Future studies would need to investigate, both numerically and experimentally, whether the BNE turns off for high oscillation frequencies or not.

In summary, we have found that the BNE occurs for the oscillation frequency and oscillation amplitude above certain values, and that critical conditions are well approximated by $\tilde{\Gamma} \gtrsim 1$ and $\tilde{v}_{\text{osc}} \gtrsim 1$ for the parameters we tested. Our results show the same general trend as other works that use comparable densities for small and large particles but assume different initial conditions otherwise. In Section 3.5, we investigate the effects of oscillations under the low-gravity environments, and discuss a possibility of having such oscillations due to impact-generated seismic waves.

3.4 Comparison with Tancredi et al. (2012)

We compared our simulations with previous works listed in Table 1 in the last subsection. We left out the results of Tancredi et al. (2012) from this discussion due to the very different oscillation style they used. In this subsection, we use initial conditions as close to theirs as we could construct, and then compare the results.

Tancredi et al. (2012) studied granular processes under various gravitational environments, and observed size segregation in response to shaking. Instead of the sinusoidal oscillation, they applied multiple vertical displacements of the floor of the simulation box at a constant speed. The duration of a displacement is $dt = 0.1$ s, and the time between displacements varies from 2–15 s, depending on the gravitational environments. The floor's speed ($v_f = 0.3 - 10 \text{ m s}^{-1}$) is linearly increased from 0 to the final value in 20 displacements. To mimic their oscillations, we do not use the vertical displacements, but instead increase the oscillation ampli-

tudes linearly so that the maximum speeds reach their final floor speeds in 20 cycles. The oscillation amplitude is chosen to be equal to one displacement $A = v_f dt$. This makes the oscillation frequency $\omega = 10 \text{ rad s}^{-1}$ for all the simulations.

Their simulation box has a size of $12 \text{ m} \times 12 \text{ m}$ and a height of 150 m. Due to the lack of viscoelastic and frictional interactions between particles and walls in their ESySPARTICLE code, they glued a layer of small particles on the floor. Since our code handles the wall-particle interactions, we do not have the glued layer.

Following their setup, we create an infinitely-tall box with the floor area of $12 \text{ m} \times 12 \text{ m}$ and fill that box with 1000 small spheres with mean radius 0.25 m and standard deviation 0.01 m as well as one large sphere with radius 0.75 m. The restitution coefficients are estimated from their sections 2.3.1–2.3.3 as follows. In the head-on collision simulation of two equal spheres (see their section 2.3.1), they obtained restitution coefficients of 0.8–0.9 for the impact speeds over $1 - 2 \text{ m s}^{-1}$. Thus, we adopt $\epsilon_n = 0.85$ for the normal coefficient of restitution between particles. In the grazing collision simulation of two equal spheres (see their section 2.3.2), they found that the ratio of final to initial speeds is ~ 0.95 for the low-speed collisions with friction. Thus, we adopt $\epsilon_t = 0.95$ for the tangential coefficient of restitution between particles. In the bouncing ball simulation against the floor with a layer of glued spheres (see their section 2.3.3), they found a coefficient of restitution of 0.593. We adopt $\epsilon_n = \epsilon_t = 0.593$ not only for the interactions between particles and the floor, but those for all the walls of the box.

The treatment of friction is also different between the codes. We chose $\mu_s = 0.6$ so that our friction constant becomes comparable to theirs at the threshold between static and dynamic friction. Since their code does not take account of rolling friction, we set $\mu_r = 0.0$.

With this setup, we performed oscillation simulations for the maximum speeds of 0.3, 1, 3, 5, and 10 m/s and show the results in Figure 10. The figure is meant to be compared with Figure 9 in Tancredi et al. (2012). Despite the differences between our codes and shaking styles, our results qualitatively agree with theirs, apart from a difference in rise time. For the low oscillation speeds (0.3 and 1 m s^{-1}), the intruder stays at the bottom of the box. As the maximum oscillation speed increases, the intruder starts rising, showing the familiar BNE. The duration of the maximum speed in our oscillation simulation (a fraction of the oscillation period of 0.63 s) is shorter than theirs. Since the rise speed is proportional to the oscillation speed (see Section 3.3), it is understandable that our results show a consistently slow rising time for the intruders compared to Tancredi et al. (2012).

3.5 Scaling in Low-gravity Environments

In this subsection, we apply our model to the low-gravity environments characteristic of asteroids. The goal here is to check whether the BNE occurs in such environments, and to understand the gravity dependence of the rise time of an intruder.

We expect that the BNE is scalable by adjusting the oscillation frequency according to the gravity field. For example, our default case has an oscillation frequency of $\omega = 3\sqrt{a_g/d_s} = 93.9 \text{ rad/s}$ under the gravitational acceleration of Earth $a_g = g = 980 \text{ cm s}^{-2}$. We change the os-

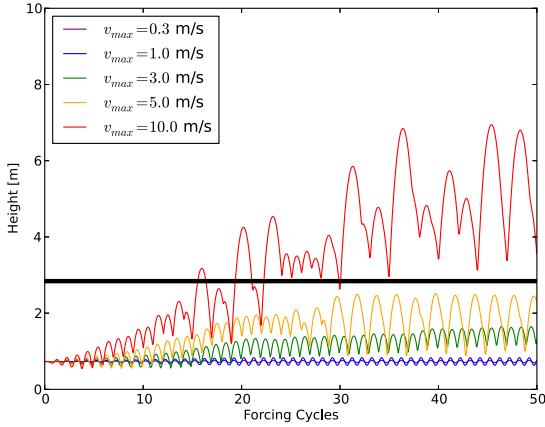


Figure 10. Evolution of the height of the intruder for the maximum oscillation speeds of 0.3, 1, 3, 5, and 10 m s^{-1} . A thick black line is drawn at a height of 2.84 m to represent the height of 1000 small particles with a random close packing and maximum bulk porosity of 0.64. The figure qualitatively agrees with Figure 9 in Tancredi et al. (2012).

cillation frequencies for the gravity fields comparable to the Moon, (1) Ceres, (87) Sylvia, Eros, and Itokawa accordingly. These bodies are chosen to compare our results with those in Tancredi et al. (2012).

We tested four different parameter sets — $(\tilde{\omega}, \tilde{A}) = (1, 0.5)$, $(1, 1)$, $(3, 1)$, and $(3, 3)$. As expected, we find that the results look similar for different gravity environments with the same scaled oscillation speeds. For $(\tilde{\omega}, \tilde{A}) = (1, 0.5)$ and $(1, 1)$, the BNE does not occur for any gravity fields, while for $(\tilde{\omega}, \tilde{A}) = (3, 1)$ and $(3, 3)$, the BNE occurs for all the cases.

The comparison of the evolution of an intruder’s height for $(\tilde{\omega}, \tilde{A}) = (3, 1)$ is plotted in Figure 11. We find that the results are all consistent with the uncertainties typical to the oscillation simulations. The figure confirms the expectation that the BNE simulations are scalable over a wide range of gravity fields.

In Figure 12, we compare our simulations under different gravity fields and the maximum oscillation speeds. The open and filled circles correspond to the runs with and without the BNE, respectively. The orange line is the critical speed we estimated in Section 3.3. As expected, BNEs are observed above \tilde{v}_c , while BNEs do not occur below the critical value.

For a comparison, we also plot BNE (open diamonds) and no-BNE cases (filled diamonds) from low-gravity simulations in Tancredi et al. (2012). Since their results also show a similar transition from no BNE to BNE around a constant \tilde{v}_c , we would expect that there is a critical floor speed necessary for the BNE in their simulations as well. Tancredi et al. (2012) estimated the floor speed threshold as $v_{\text{thre}} = 1.12a_g^{0.42}$, which has a slightly different dependency on the gravitational acceleration from our relation of $v_c \sim \sqrt{d_s a_g}$. This difference may not be surprising since threshold speeds in Tancredi et al. (2012) are determined by relatively sparse data.

It is also informative to plot the rise speed of an intruder as a function of the gravity field. Figure 13 shows

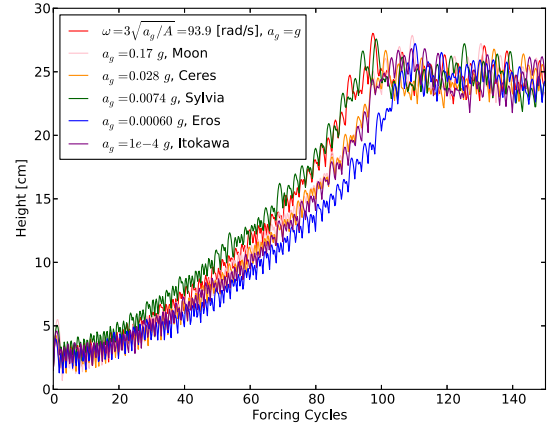


Figure 11. Evolution of height of the intruder as a function of oscillation cycles for the gravities of Earth, Moon, Ceres, Sylvia, Eros, and Itokawa.

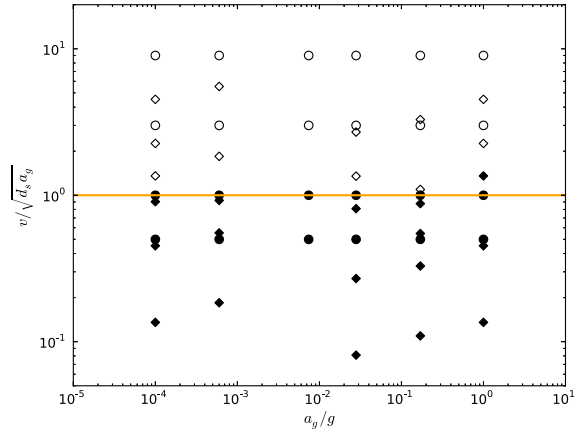


Figure 12. The scaled oscillation speeds compared with the scaled gravitational acceleration. The solid orange line corresponds to the critical speed $\tilde{v}_c = 1.0$ estimated in Section 3.3. Open and filled symbols correspond to BNE and no-BNE cases in our simulations (circles) and in Tancredi et al. (2012) (diamonds). For data from Tancredi et al. (2012), we simply follow their Figure 11 to distinguish BNE and no-BNE cases.

that, for both $(\tilde{\omega}, \tilde{A}) = (3, 1)$ and $(3, 3)$, the rise speed is proportional to $\sqrt{a_g}$, rather than a_g . This is understandable in our case, since the driving frequency of our oscillation simulations is $\omega \propto \sqrt{a_g}$. The result is consistent with our finding in Section 3.3 that the rise speed is proportional to the maximum oscillation speed.

Recently, Güttler et al. (2013) experimentally studied the BNE both in the laboratory and in a parabolic flight to mimic the reduced-gravity conditions comparable to Mars and the Moon. They found that the rise speed was not proportional to $\sqrt{a_g}$, but closer to a_g . In fact, their best fit was obtained for an exponential function. The difference seen in our rise speed dependences with gravity may be partly due to the difference in our shaking profiles. While we use a sinusoidal oscillation, their oscillation acceleration is ap-

proximated by a square-wave function. Moreover, due to the nature of a parabolic flight, they need to stop the oscillations every time the hyper-gravity phase kicks in, which could have compacted the particle distributions and slowed the rise of an intruder. Future studies need to investigate the dependence of rise speed (or equivalently rise time) on the gravity field further.

Finally, we estimate the critical oscillation speeds of the BNE for observed asteroids. From the critical conditions confirmed in Section 3.3, we can derive two conditions for critical oscillation speeds,

$$\tilde{v}_c \gtrsim 1.0 \rightarrow v \gtrsim \sqrt{d_s a_g}, \text{ and} \quad (2)$$

$$\tilde{\Gamma}_c \gtrsim 1.0 \rightarrow v \gtrsim \sqrt{A a_g}. \quad (3)$$

In Figure 14, we plot these conditions for Itokawa (left panel) and Eros (right panel) by assuming three different diameters for a typical small particle (1, 10, and 100 cm). When the particle size is $d_s = 10$ cm, the oscillation speeds need to be larger than $v_c \sim 1 \text{ cm s}^{-1}$ for the BNE to take place on Itokawa, and larger than $v_c \sim 2.5 \text{ cm s}^{-1}$ on Eros. Thus, as expected from the relation $v_c \propto \sqrt{a_g}$, size segregations occur for weaker oscillations on smaller asteroids.

The upper limit of the BNE oscillation speeds can be set by the escape speed. The escape speeds are $\sim 16.5 \text{ cm s}^{-1}$ for Itokawa and $\sim 9.71 \text{ m s}^{-1}$ for Eros, and are plotted as black solid lines in Figure 14 (note that the latter line overlaps with the top boarder of the panel). For a small asteroid like Itokawa that has a diameter < 500 m, the BNE is allowed only for small oscillation amplitudes $\lesssim 10$ m if a typical small particle size is 100 cm. For smaller particles, a wider range of conditions is possible. For a larger asteroid like Eros that has a diameter of ~ 20 km, a typical small particle size can be larger than 100 cm.

How do these oscillation speeds compare to the characteristic seismic speeds in asteroids? From Asphaug et al. (1996), the estimated critical oscillation speeds are consistent with the speeds of seismic motions that could create bright annuli around craters on small asteroids such as Ida. We estimate the critical seismic speeds below and plot them in Figure 14 as solid and dashed green lines.

The impact energy of a projectile can be written as

$$E_i = \frac{2\pi}{3} \rho_p R_p^3 v_p^2, \quad (4)$$

where p denotes the projectile, ρ is the density, R is the spherical radius, and v_p is the impact speed. Following Richardson et al. (2005), we also write the total seismic energy of an asteroid due to a seismic wave speed v_s as

$$E_s = \frac{2\pi}{3} \rho_t R_t^3 v_s^2. \quad (5)$$

Here, t denotes the target asteroid and $v_s = 2\pi f A$, where f and A are the seismic frequency and maximum displacement, respectively, from Richardson et al. (2005). More complex representations may be appropriate for purely agglomerate bodies, but since there is no good understanding of the actual structure of agglomerate asteroids or the transmission of seismic waves within such a medium, we have assumed that the waves are transmitted in a simplified fashion (i.e., a sinusoidal oscillation).

When a fraction η of the kinetic energy of an impactor is converted into seismic energy (i.e., $E_s = \eta E_i$), the seismic speed v_s on an asteroid is estimated as

$$v_s = \sqrt{\eta \frac{\rho_p}{\rho_t} \left(\frac{R_p}{R_t} \right)^3} v_p \quad (6)$$

By defining a specific impact energy as

$$Q_s = \frac{1}{2} \frac{\rho_p}{\rho_t} \left(\frac{R_p}{R_t} \right)^3 v_p^2, \quad (7)$$

we can rewrite a seismic speed as $v_s = \sqrt{2\eta Q_s}$.

To estimate a seismic speed for a certain impact, we consider an extreme case where an impact leads to a catastrophic disruption (i.e., an impact that results in the largest remnant having half the mass of the original target) and define the specific impact energy as $Q_s = Q_{s,D}$. Jutzi et al. (2010) performed numerical simulations of asteroid break-ups, and estimated such specific energy threshold for disruption $Q_{s,D}$. They provided the following convenient power-law scaling:

$$Q_{s,D} = Q_0 \left(\frac{R_t}{\text{cm}} \right)^\alpha + B \rho_t \left(\frac{R_t}{\text{cm}} \right)^\beta, \quad (8)$$

where Q_0 , B , α , and β are fitting constants. The first term represents the strength regime where fragments are held together by material strength alone, and the second term represents the gravity regime where fragments are gravitationally bound. The transition between these two regimes is estimated to occur for target diameters between 100 and 200 m (Benz & Asphaug 1999). The fitting constants depend on a variety of parameters such as internal structures, tensile and shear strengths of constituents, and impact speeds. Jutzi et al. (2010) considered two models for the target's internal structure — a purely monolithic non-porous target and a porous target that consists of a body with pores that are smaller than the thickness of the shock front, and determined the fitting constants for impact speeds of 3 and 5 km s^{-1} . Since both Itokawa and Eros have low bulk densities compared to ordinary chondrites (Wilkinson et al. 2002; Fujiwara et al. 2006), we adopt the fitting parameters for a porous target. By assuming impact seismic efficiency of $\eta = 10^{-4}$ (Richardson et al. 2005, and references therein), we plot critical seismic speeds v_s for impact speeds of 3 and 5 km s^{-1} as dashed and solid green lines, respectively, in Figure 14. Regions below these lines correspond to seismic speeds expected for smaller impactors that will not destroy the asteroids.

For Itokawa, we find that critical seismic speeds would be comparable to, but slightly larger than, the escape speed, and larger than the minimum oscillation speeds required for the BNE. For Eros, critical seismic speeds would be smaller than the escape speed, but they are still larger than the estimated minimum oscillation speeds. Thus, in both cases, we expect that the critical BNE oscillation speeds are comparable to the seismic speeds that can create craters.

It is also informative to speculate how long it might take for a large block to rise to the surface of an asteroid. From Figure 9, we find that the rise speed of an intruder is more than an order of magnitude slower than the maximum oscillation speed for these three bed depths. Assuming an oscillation speed of 1 cm s^{-1} and a depth of 100 m from the shortest axis of Itokawa of ~ 200 m, we can estimate that the rise time would be a few hours if the rise speed is comparable to the oscillation speed, and more than a day if the rise speed is one tenth of the oscillation speed. Similarly, by assuming

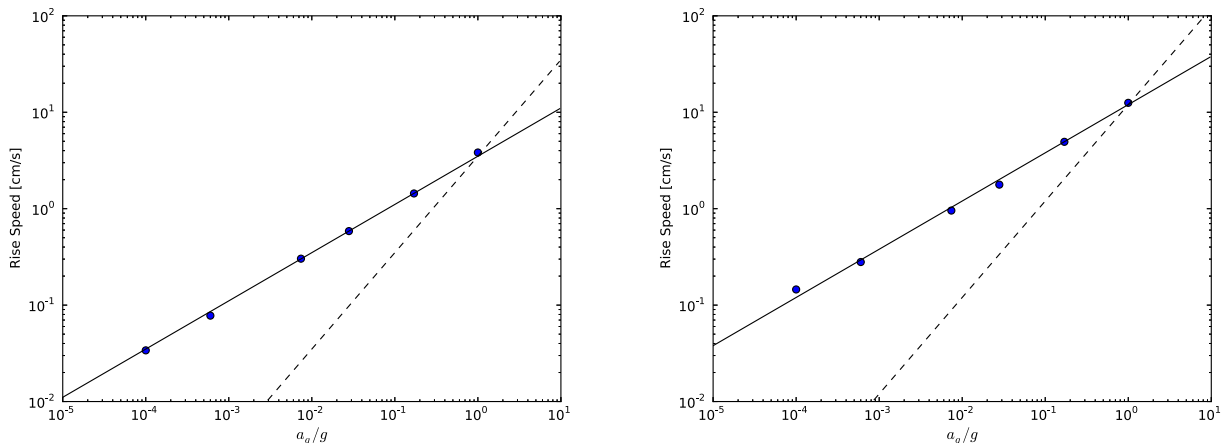


Figure 13. Change of the rise speed of an intruder depending on the gravity field. Left and right panels correspond to $(\tilde{\omega}, \tilde{A}) = (3, 1)$, and $(3, 3)$, respectively. Solid and dashed lines are proportional to $\sqrt{a_g}$ and a_g , respectively. The rise speeds of both sets of our simulations have a $\sqrt{a_g}$ dependence.

an oscillation speed of 100 cm s^{-1} and a depth of 5.5 km from the shortest axis of Eros of $\sim 11 \text{ km}$, the rise time would be about 90 minutes for the oscillation speed, and about 15 hours for one tenth of that speed. This implies that unless the seismic shaking lasts for more than a couple of hours, one impact might not be enough for a large block to rise to the surface, and that multiple impacts would be necessary to change the surface significantly.

A potential problem for size sorting by multiple impacts is that the oscillation directions will likely vary for different impacts. To check this point, we performed simulations where we changed the direction and magnitude of *effective* gravity instead of oscillating cylinders sinusoidally. First, we consider the most ideal case where the impact is always applied in the vertical direction of the cylinder. We use the initial conditions identical to the default case, and change only the direction of the gravity as follows. Initially, the gravity is in the $-z$ direction with the magnitude of the Earth’s gravity. Once the simulation starts, we apply a “jolt” to the cylinder by changing the gravity vector first to the $+z$ direction and then back to the $-z$ direction within a short period of time that is randomly chosen from $0.1 - 0.3 \text{ s}$. We then keep on applying the Earth gravity in the $-z$ direction for a randomly chosen period of time from $0.3 - 0.4 \text{ s}$. After this break, we again apply a jolt as described above, and repeat these steps a number of times. Here, the choice of the duration of the jolts is arbitrary. In this set up, we find that the intruder comes to the surface within $\sim 20 \text{ s}$, which is comparable to the rise time of the low-speed oscillation (e.g., $\tilde{\omega} = 1.0$ and $\tilde{A} = 2.0$). Next, we consider a less ideal case where the impact is applied in a random direction relative to the cylinder. Similar to the above case, the cylinder is initially under Earth’s gravity in the $-z$ direction. To mimic a jolt, we randomly choose the gravity magnitude from $-2g$ to $2g$ in each direction of x , y , and z , and smoothly change the magnitude and direction of the gravity vector from and then back to the initial one within $0.1 - 0.3 \text{ s}$. After the break of $0.3 - 0.4 \text{ s}$, we apply another random jolt and repeat these steps a number of times. We find that the rise of the intruder is much slower in this setup. After $\sim 180 \text{ s}$, the intruder is

about one quarter of the bed depth from the bottom of the cylinder. Therefore, we expect that the rise time would be much longer than the ones estimated from our sinusoidal oscillations if the oscillations are applied from random directions. If, on the other hand, the oscillations are applied approximately perpendicular to a particle bed, the rise time would be less affected.

4 DISCUSSION AND CONCLUSIONS

We have studied the BNE in an intruder model by using the N -body code PKDGRAV with a soft-sphere collision model, and explored its effect on asteroids. We have also investigated the dependence of the BNE on the particle properties, oscillation conditions, and gravitational environments.

Similar to previous studies, we have found that convection is the major driving source for the BNE. Our main conclusions are the following.

- (i) The occurrence of the BNE as well as the rise time of an intruder is largely independent of the choice of coefficients of restitution (see Section 3.1). For highly elastic particles ($\epsilon \gtrsim 0.9$), however, the rise time might differ significantly from less elastic cases.
- (ii) The occurrence of the BNE depends on the values of friction constants (see Section 3.2). Both too high and too low friction constants diminish convection and thus the BNE.
- (iii) The critical condition for the BNE agrees well with the limits of $\tilde{\Gamma} \gtrsim 1$ and $\tilde{v}_{osc} \gtrsim \tilde{v}_c \sim 1$ (see Section 3.3). These conditions also agree well with previous simulations and experiments that have comparable densities for small and large particles.
- (iv) The BNE is scalable for different gravitational environments by choosing the oscillation frequency that corresponds to the gravitational acceleration (i.e., $\omega \propto \sqrt{a_g}$, see Section 3.5). Thus, the same level of size sorting is expected for a smaller oscillation speed on a small asteroid compared to a big one.

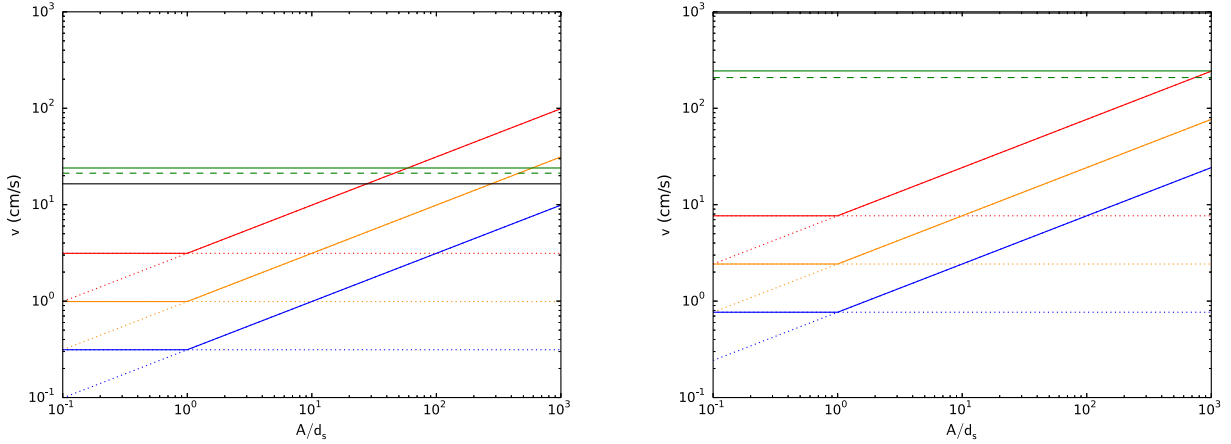


Figure 14. The critical oscillation speeds necessary for the BNE that is estimated from $\tilde{\Gamma}_c = 1.0$ and $\tilde{v}_c = 1.0$ for Itokawa (left panel) and Eros (right panel). Blue, orange, and red lines correspond to a typical small particle’s size of 1, 10, and 100 cm, respectively. Green solid and dashed lines are the seismic speeds estimated from an impact that lead to a catastrophic disruption, and correspond to the impact speeds of 5 km s^{-1} and 3 km s^{-1} , respectively. Larger projectiles would destroy asteroids (above these lines), while smaller ones would generate seismic speeds (below these lines) that are comparable to the critical oscillation speeds for the BNE. The solid black line is the escape speed.

(v) The rise speed of an intruder is proportional to the oscillation speed (see Sections 3.3 and 3.5). Also, there might be an optimal bed depth for a certain oscillation speed to achieve the fast rise of an intruder.

(vi) For a wide cylinder, the convection roll along the wall may be thick enough to pass the intruder downward, leading to a “whale” effect (see Section 3.3).

(vii) The BNE is expected to occur on an asteroid for seismic speed that is comparable to non-destructive impacts (see Section 3.5). We have compared the critical oscillation speed for the BNE with the critical seismic speed, and found that the region for the BNE overlaps with that of the seismic shaking.

(viii) We also estimate the rise time of a large block from the central region to the surface of an asteroid, and predict that multiple impacts or long-lasting seismic shaking might be required for the BNE to significantly change the asteroid surface. A potential problem which could affect such multiple impacts is that the BNE might slow down significantly for randomly oriented oscillations.

The efficiency of the BNE depends on many properties. In this paper, we have explored the dependence on the coefficients of restitution, the friction constants, the oscillation frequency and amplitude, the particle bed depth, and the gravity. One of the potential directions for the future study would be to investigate how the BNE changes from the dense limit to the vibro-fluidized regime. In particular, it would be interesting to perform the BNE experiments in the high-speed region to understand whether the BNE keeps on occurring as our code predicts, or turns off sharply as suggested by Godoy et al. (2008).

The rise time of an intruder is important to estimate the efficiency of the BNE on asteroids. Our work shows that the rise speed linearly scales with the oscillation speed and is proportional to $\sqrt{a_g}$. Although this result is intuitive, we should check whether such a trend would hold for different shaking models as well since most of our simulations

assume sinusoidal oscillations. Interestingly, the analytical model developed by Jiongming et al. (1998) also estimates that the rise speed is proportional to $\sqrt{a_g}$.

In this paper, we did not mention the effects of the particle’s size distribution, the container width, or the container shape. We assume the idealized system where all of the small particles have the same size (except for Section 3.4) and the size ratio of large to small particles is $d_l/d_s = 3$. However, particles in actual asteroids will generally follow some size distribution. Previous studies have shown that the BNE occurs only for a radius ratio of large and small particles greater than some threshold (e.g., Duran et al. 1994; Vanel et al. 1997). The size ratio we chose for our simulations ($d_l/d_s = 3$) is near the threshold according to these experiments. Thus, we expect that the size ratio might need to be near this value or larger for the BNE to take place. Also, a preliminary study we performed indicates that the rise speed of an intruder slows down when a size distribution of small particles is introduced. Such effects on the rise speed should be studied more carefully in future work.

Differences due to the container could also be significant. The experimental studies by Hejmady et al. (2012) suggest that both bed heights and widths affect the rise time of an intruder. Furthermore, previous studies have shown that “reverse” convection (i.e., in which the particle flow ascends along the wall and descends around the center) is seen for granular materials in a container with outwardly slanting walls (e.g., Grossman 1997) and thus the intruder is trapped at the bottom rather than at the bed surface in such a container (e.g., Knight et al. 1993). Indeed, when we use a bowl instead of a cylinder as a container, we observe that the intruder goes up and down in the granular bed, but never comes to the surface for a density ratio of $\rho_l/\rho_s = 1$. Our further tests with $\rho_l/\rho_s = 0.5$ and 2 show that the BNE occurs for the former, but not for the latter. The rise of the intruder in the former case is consistent with the expected behavior of the normal fluid. There is a related issue when

we consider the BNE in an asteroid. The BNE requires the container wall to create the convective flow, but there is no actual wall such as the ones we considered here in an asteroid. However, it is plausible that a very large body could act as a wall for the smaller particles. For future work, we intend to investigate the effect of having no lateral walls by adopting periodic boundary conditions, and also to improve our current study by modelling self-gravitating rubble piles.

One of the most important fundamental problems is the absence of knowledge of the coefficients of restitution and friction constants of particles in asteroids. Currently, our knowledge of these values relies on experiments, for example, the collision experiment done by Durda et al. (2011) on 1 m-size granite spheres or the avalanche experiment done by Yu et al. (2014) with gravels. However, it is not clear whether such objects have the same mechanical behavior as materials composing asteroids of interest. There are some future missions that are expected to return asteroid samples, such as Hayabusa 2, OSIRIS-REx, and potentially MarcoPolo-R. These efforts will lead to a better understanding of surface features and will provide invaluable knowledge of asteroid compositions as well as their response to external solicitations, such as that of the sampling tool.

ACKNOWLEDGEMENTS

We thank Carsten Güttler for useful discussions, and the referee, Gonzalo Tancredi, for careful reading and detailed comments. SM is supported by an Astronomy Center for Theory and Computation Prize Fellowship at the University of Maryland, and also by the Dundee Fellowship at the University of Dundee. PM and SRS acknowledge support from the french space agency CNES. All of the simulations in this paper were done on the YORP cluster in the Department of Astronomy at UMD and on the Deepthought High-Performance Computing Cluster at UMD. This material is based partly on work supported by the US National Aeronautics and Space Administration under Grant Nos. NNX08AM39G, NNX10AQ01G, and NNX12AG29G issued through the Office of Space Science and by the National Science Foundation under Grant No. AST1009579.

REFERENCES

- Asphaug E., King P. J., Swift M. R., Merrifield M. R., 2001, in *Lunar and Planetary Institute Science Conference Abstracts Vol. 32 of Lunar and Planetary Institute Science Conference Abstracts, Brazil Nuts on Eros: Size-Sorting of Asteroid Regolith*. p. 1708
- Asphaug E., Moore J. M., Morrison D., Benz W., Nolan M. C., Sullivan R. J., 1996, *Icarus*, 120, 158
- Asphaug E., Ryan E. V., Zuber M. T., 2002, *Asteroids III*, pp 463–484
- Benz W., Asphaug E., 1999, *Icarus*, 142, 5
- Breu A. P., Ensner H.-M., Kruelle C. A., Rehberg I., 2003, *Physical Review Letters*, 90, 014302
- Chapman C. R., 2004, *Annual Review of Earth and Planetary Sciences*, 32, 539
- Clément E., Duran J., Rajchenbach J., 1992, *Physical Review Letters*, 69, 1189
- Duran J., Mazozi T., Clément E., Rajchenbach J., 1994, *PhRvE*, 50, 5138
- Durda D. D., Movshovitz N., Richardson D. C., Asphaug E., Morgan A., Rawlings A. R., Vest C., 2011, *Icar*, 211, 849
- Fujiwara A., Kawaguchi J., Yeomans D. K., Abe M., Mukai T., Okada T., Saito J., Yano H., Yoshikawa M., Scheeres D. J., Barnouin-Jha O., Cheng A. F., Demura H., Gaskell R. W., Hirata N., Ikeda H., Kominato T., Miyamoto H., Nakamura A. M., Nakamura R., Sasaki S., Uesugi K., 2006, *Science*, 312, 1330
- Godoy S., Riso D., Soto R., Cordero P., 2008, *PhRvE*, 78, 031301
- Grossman E. L., 1997, *PhRvE*, 56, 3290
- Güttler C., von Borstel I., Schräpler R., Blum J., 2013, *PhRvE*, 87, 044201
- Hejmady P., Bandyopadhyay R., Sabhapandit S., Dhar A., 2012, *PhRvE*, 86, 050301
- Hsiao S., Yu H., 1997, *Powder Technology*, 93, 83
- Huerta D. A., Ruiz-Suárez J. C., 2004, *Physical Review Letters*, 92, 114301
- Jiongming S., Binglu S., Bin W., 1998, *Nuovo Cimento D Serie*, 20, 1443
- Jutzi M., Michel P., Benz W., Richardson D. C., 2010, *Icarus*, 207, 54
- Knight J. B., Jaeger H. M., Nagel S. R., 1993, *Physical Review Letters*, 70, 3728
- Kudrolli A., 2004, *Reports on Progress in Physics*, 67, 209
- Liffman K., Muniandy K., Rhodes M., Gutteridge D., Metcalfe G., 2001, *Granular Matter*, 3, 205
- Michel P., O'Brien D. P., Abe S., Hirata N., 2009, *Icarus*, 200, 503
- Michel P., Richardson D. C., 2013, *A&A*, 554, L1
- Miyamoto H., Yano H., Scheeres D. J., Abe S., Barnouin-Jha O., Cheng A. F., Demura H., Gaskell R. W., Hirata N., Ishiguro M., Michikami T., Nakamura A. M., Nakamura R., Saito J., Sasaki S., 2007, *Science*, 316, 1011
- Ohtsuki T., Kinoshita D., Takemoto Y., Hayashi A., 1995, *Journal of the Physical Society of Japan*, 64, 430
- Pöschel T., Herrmann H. J., 1995, *EPL (Europhysics Letters)*, 29, 123
- Richardson D. C., Leinhardt Z. M., Melosh H. J., Bottke Jr. W. F., Asphaug E., 2002, *Asteroids III*, pp 501–515
- Richardson D. C., Michel P., Walsh K. J., Flynn K. W., 2009, *P&SS*, 57, 183
- Richardson D. C., Quinn T., Stadel J., Lake G., 2000, *Icarus*, 143, 45
- Richardson D. C., Walsh K. J., Murdoch N., Michel P., 2011, *Icar*, 212, 427
- Richardson J. E., Melosh H. J., Greenberg R. J., O'Brien D. P., 2005, *Icarus*, 179, 325
- Riso D., Soto R., Godoy S., Cordero P., 2005, *PhRvE*, 72, 011305
- Rosato A., Strandburg K. J., Prinz F., Swendsen R. H., 1987, *Physical Review Letters*, 58, 1038
- Saez A., Vivanco F., Melo F., 2005, *PhRvE*, 72, 021307
- Sanders D. A., Swift M. R., Bowley R. M., King P. J., 2004, *Physical Review Letters*, 93, 208002
- Schwartz S. R., Michel P., Richardson D. C., 2013, *Icarus*, 226, 67
- Schwartz S. R., Michel P., Richardson D. C., Yano H., 2014, submitted to *Plan. & Space Sci.*

- Schwartz S. R., Richardson D. C., Michel P., 2012, *Granular Matter*, 14, 363
- Shishodia N., Wassgren C. R., 2001, *Physical Review Letters*, 87, 084302
- Stadel J. G., 2001, PhD thesis, UNIVERSITY OF WASHINGTON
- Tancredi G., Maciel A., Heredia L., Richeri P., Nesmachnow S., 2012, *MNRAS*, 420, 3368
- Vanel L., Rosato A. D., Dave R. N., 1997, *Physical Review Letters*, 78, 1255
- Wilkison S. L., Robinson M. S., Thomas P. C., Veverka J., McCoy T. J., Murchie S. L., Prockter L. M., Yeomans D. K., 2002, *Icarus*, 155, 94
- Yu Y., Richardson D. C., Michel P., Schwartz S. R., Ballouz R.-L., 2014, submitted to *Icarus*